Experimental analysis on the effects of DC arc discharges at various flow regimes

G. Bianchi, B. H. Saracoglu, G. Paniagua, and T. Regert

Citation: Physics of Fluids (1994-present) **27**, 036102 (2015); doi: 10.1063/1.4914868
View online: http://dx.doi.org/10.1063/1.4914868
View Table of Contents: http://scitation.aip.org/content/aip/journal/pof2/27/3?ver=pdfcov
Published by the AIP Publishing

PHYSICS OF FLUIDS **27**, 036102 (2015)

Experimental analysis on the effects of DC arc discharges at various flow regimes

G. Bianchi,[1] B. H. Saracoglu,[2,a)] G. Paniagua,[3] and T. Regert[2]
[1]*University of L'Aquila, L'Aquila 67100, Italy*
[2]*von Karman Institute for Fluid Dynamics, Rhode Saint Genèse B-1640, Belgium*
[3]*Purdue University, West-Lafayette, Indiana 47907, USA*

(Received 19 August 2014; accepted 2 March 2015; published online 18 March 2015)

This paper addresses the control of the boundary layer on a compression ramp by means of DC electrical arc discharges. The development and realization of the control system are first described and then assessed in the wind tunnel. The objective of the research was to control the supersonic flow using the minimum amount of energy. The array of electrodes was located at the base of a ramp, where a low momentum flow develops. The electrical discharge was generated by a custom designed electronic facility based on high-voltage ignition coils. The slanted tungsten electrodes were insulated by mounting them in a ceramic support. The discharge evolution was studied through high-speed flow visualizations, while electrical measurements at the high-voltage section of the circuitry allowed to estimate the energy release. The development of a high-speed short exposure Schlieren imaging technique, based on a very short duration laser pulse illumination and a double shot CCD camera, allowed to observe the macroscopic effects associated with the arc establishment between the electrodes (glow, sound wave and heat release). Due to the long residence time, the thermal perturbation spread along the streamwise direction. Cross correlation of Schlieren images with short time separation revealed that in supersonic conditions, the discharges led to an overall acceleration of the flow field underneath the oblique shock wave. [http://dx.doi.org/10.1063/1.4914868]

I. INTRODUCTION

When high voltage is established in between two electrodes, an arc occurs across the electrode gap.[1] The induced avalanche mechanism ends up with the creation of a highly conductive channel, sustained by the thermionic effect that enhances the ionization rate.[2,3] The de-excitation of the electrons that collide with the gas leads to photon emission, thus the glow of the arc. Simultaneously, the Joule effect implies a sudden temperature rise that creates compression waves which in turn degenerate to a shock wave and thus to an audible sound.[4] The hot region expands because of the conductive heat exchange with the encircling colder flow.[5] Consequently, the macroscopic effects associated with arc discharges are light emission, pressure fluctuations, and thermal phenomena, all with characteristic speeds that differ by several orders of magnitude.

In the current work, the macroscopic effects induced by the arc discharge were investigated with the purpose of aerodynamic flow control. Among the active flow control techniques that aim at manipulating a flow field through direct energy supply, electrical discharges have recently acquired a growing interest because of the freedom of tuning the actuations in terms of power and frequency.[6] The control mechanisms related to arc discharges are of three types, namely, electro-hydrodynamic[7] (EHD), magneto-hydrodynamic[8] (MHD), and thermal.[9] The interaction of the thermal effects with

a)Author to whom correspondence should be addressed. Electronic mail: saracog@vki.ac.be

the flow field has been previously exploited in supersonic applications, such as starting issues in supersonic inlets and mixing enhancement in supersonic combustors. Leonov *et al*. reported significant changes in the flow topology by means of a quasi-DC array of electrical discharges to control the diffuser performance and to improve combustor efficiency at supersonic regimes.[10,11] Samimy *et al*. extensively investigated the development of localized arc filament plasma actuators in supersonic applications.[12,13] A very rapid local heating produced pressure perturbations that acted as a solid obstacle placed into the flow. Repetitive pulsations of the discharge, whose frequency was tuned with the instabilities of the flow, showed a significant effect in jets concerning the noise mitigation and combustion enhancement and, recently, in shock wave boundary layer interaction in supersonic diffusers. Elliott and Dutton provided experimental evidence of the effects of different types of plasma actuators at different flow speeds.[14–16]

This paper presents the design of an actuator device in which an array of three electrode pairs is able to supply discharges perpendicularly to the flow direction and without erosion. An electronic circuit based on ignition coils further guaranteed their synchronization, a fundamental requirement to maximize the effectiveness of the actuation.[17] The capabilities of the technique were assessed through measurements at different flow speeds: quiescent, low subsonic, and supersonic at Mach 3.3. To overcome the constraints related to the capture of the discharge evolution and its macroscopic effects, a high speed short exposure Schlieren technique was developed based on a pulsed laser illumination and a double shot Particle Image Velocimetry (PIV) camera.[18]

II. EXPERIMENTAL METHODOLOGY

Modulation of the flow topology through electrical discharges required a preliminary study of the different subsystems. A DC arc discharge generator based on an automotive ignition system was designed and tested. Current and high voltage measurements were used to track the discharge evolution and the resulting energy release. Preliminary studies on a support made of a polyamide based material, commercially known as Vespel, equipped with steel electrodes urged a new design, with an enhanced dielectric strength (machinable ceramic) and higher melting temperature electrodes (tungsten) to prevent erosion.[19] The upgraded configuration provided the alignment of multiple discharges in the transversal direction of the wind tunnel. This array was then installed upstream of a wedge and used to create aerodynamic perturbations. Pressure measurements allowed to characterize the flow both upstream and downstream of the actuators, while high speed Schlieren visualizations provided a direct indication about the flow topology. The fast dynamics of the discharges together with the high mean flow velocity eventually led to the development of a high speed short exposure Schlieren imaging system, based on the hardware setup of a PIV system.

A. Test rig

The experiments were carried out in a supersonic blow-down wind tunnel at the von Karman Institute. It consists of a contoured converging-diverging nozzle that allows to reach a freestream Mach number of 3.3, a Reynolds number per unit length of 5×10^7/m, with a yielded flow enthalpy equal to 30 J. The 80 mm wide test section is composed of two parallel aluminum flat plates separated by 100 mm (Figure 1(a)). The bottom one hosts the electrode module in the central region, 10 mm upstream of a ramp with a contraction ratio at the throat of 83.9% and a wedge angle of 23.5° (Figure 1(b)). This angle was selected to ensure that, in supersonic test conditions, the ramp became a self-started supersonic diffuser with an oblique shock wave anchored upstream of it. The flow facing surfaces of the wind tunnel were hand polished, resulting in a peak-to-peak roughness quality of 1.6 μm such that unintentional compression waves in supersonic flows and optical reflections that might have reduced the quality of the flow visualizations were prevented. The streamwise Mach number evolution was monitored with a Pitot probe in the settling chamber and static pressure measurements at the bottom plate and along the ramp, as shown in Figure 1(c).

Figure 1(d) illustrates the discharges at M = 3.3 flow conditions; during the supersonic experiments, a secondary discharge was observed between the electrodes and the rear part of the test

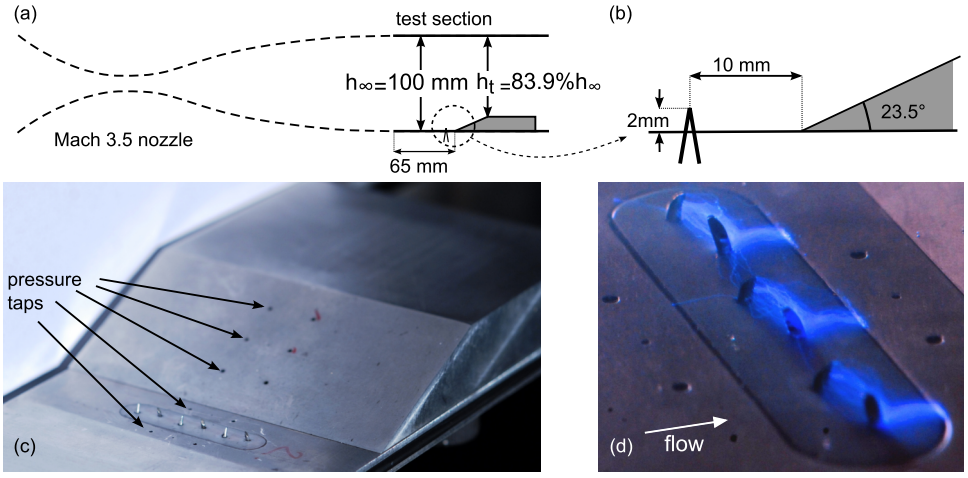

FIG. 1. Schematics of the wind tunnel setup: (a) nozzle and test section, (b) streamwise electrodes arrangement, (c) measurement locations, (d) discharges at Mach 3.3.

section. In previous experiments, Leonov *et al.*[11] observed that the flow may stretch the arc downstream, eventually collapsing and giving rise to a new arc, inducing an unsteady blowdown phenomena. In the present experiments, however, the actuator arced during less than 4 μs, and we did not observe such an unsteady blowdown effect. The spreading of the arc along the supersonic streamwise direction can be reduced using a larger dielectric support, to prevent the abatement of the energy addition at the intended axial location. The existence of the secondary arc, and thus variance in the discharge characteristics, prevents a direct comparison of the quiescent, subsonic, and supersonic results regarding the mechanism of the actuation.

B. Electrode array

Figure 2 depicts the light emission captured by a Phantom v7.1 high-speed camera (with a 55 mm 1:2.8 aperture micro objective) in the preliminary tests performed on a polyamide substrate with blunt steel electrodes. After the arc (15 μs), the glow between the electrodes gradually vanishes, although the tips were still visible because of the overheating due to the Joule effect. At about 100 μs, it was observed that the degree of overheating increased and the melting point of the steel was locally reached at the right electrode (cathode). Cathode sputtering[1] occurred through some

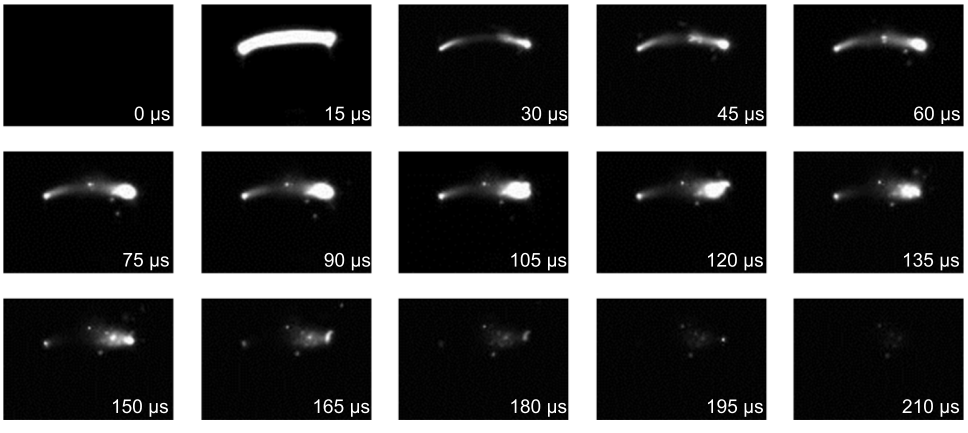

FIG. 2. Discharge evolution in a polyimide-based plastics support with steel electrodes 128×104 pixels, f_s 67 kHz, exposure time 10 μs.

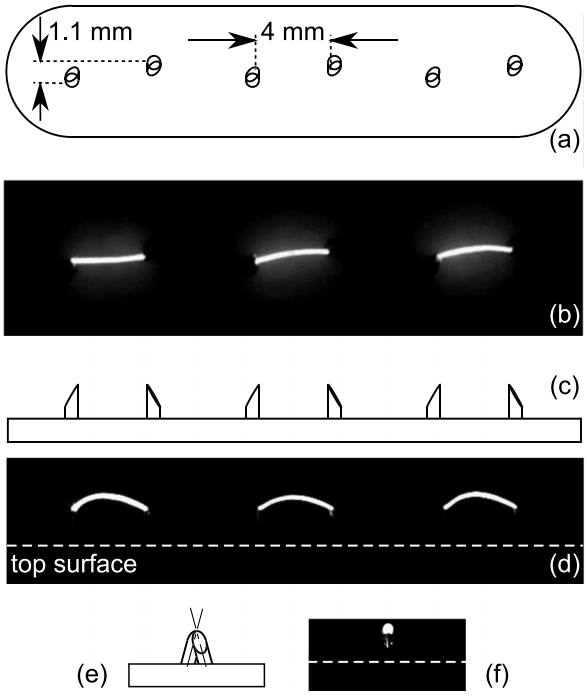

FIG. 3. Design and experimental assessment of the discharge synchronization and alignment from top (a), (b), frontal (c), (d), and side (e), (f) views.

material that was chipped off from the electrode with a mean particle velocity of 18.9 m/s. The subsequent cooling by the surrounding air (at ambient temperature) eventually became predominant, and hence, the brightness of the electrode tips diminished. The residence time of the discharge after the arc regime was estimated to be 120 μs.

The frame series assessed a quick aging of the electrodes due to the high temperatures reached during the arc regime. In consequence, the electrodes suffered erosion, while the polyimide-based plastics support was burnt. To overcome these issues, the discharge device was redesigned using a machinable glass ceramic support to maximize the insulation and tungsten electrodes to prevent aging. Figure 3(a) displays the final arrangement with an electrode gap equal to 4 mm and 5 mm distance between neighbouring electrode pairs. Furthermore, the electrode tips were sharpened to enhance the density charge at these points thus reducing the breakdown threshold (Figure 3(c)). As can be noticed from Figure 3(e), in each pair, the positive and negative electrodes were 15° slanted in opposite directions inside the support, such that the minimum distance was reached between the tips. Magnified top, frontal, and side views of the electrode module during the discharge taken with the high-speed camera and the micro objective are reported in Figures 3(b), 3(d), and 3(f), respectively, and exhibit discharge alignment and synchronization.

The electrodes tips were set 2 mm above the bottom plate, to supply the discharges within the boundary layer, with a blockage effect constrained to 0.12%. The actuators were centered in the test section to allow the interaction with the two-dimensional flow.

C. Electronic circuit

The electronic system able to generate synchronized DC discharges relies on automotive ignition coils that are connected in parallel to supply the same voltage to all the actuators, as shown in Figure 4. The ratio between the primary (low-voltage) and secondary windings (high-voltage) of the coils allows to generate high voltages from a 12 V DC battery. The voltage at the primary windings was varied in time according to a square wave with a duty cycle of 50% generated by a 555 timer. The actuation frequency could be tuned through a multi-turn potentiometer from 0.7 to 35 Hz. The square

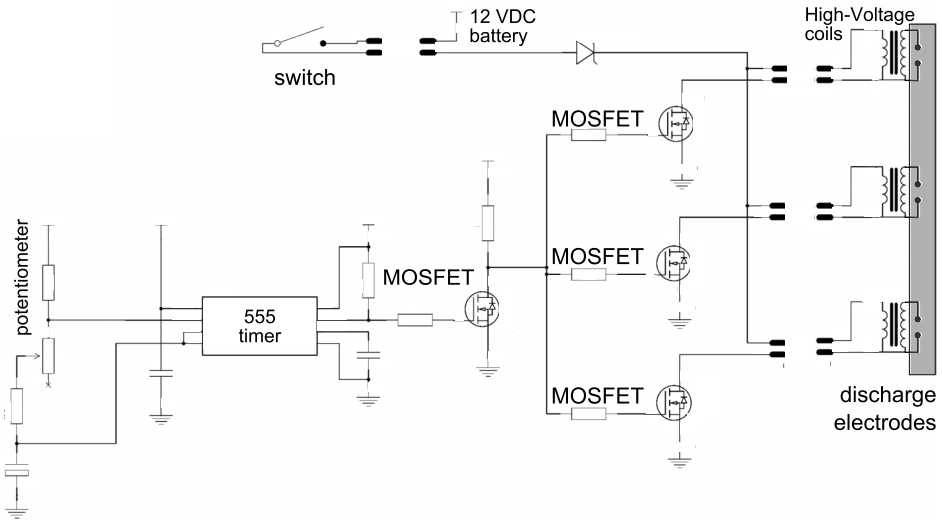

FIG. 4. Circuitry diagram.

wave excited the gate of a MOSFET transistor that became conductive and further triggered similar devices connected upstream of the primary windings of each coil. The resulting voltage change was amplified at the secondary windings and allowed for the breakdown conditions across the electrodes. Discharge frequencies of about 300 Hz could be attained by replacing the 555 timer with an oscillating device based on an Insulated Gate Bipolar Transistor (IGBT) transistor and an aluminum electrolytic capacitor. The IGBT polarization may be tuned with a dedicated driver module triggered by a function generator. In order to achieve frequencies beyond a kHz, the power source voltage should be increased to allow a faster recharge of the coil, otherwise the discharge breakdown might be not reached.

The circuit performance was characterized by means of electrical measurements at the low and high voltage sections of the circuit. In the latter, a ground-referenced voltage probe (Tektronix P6015A) and a Hall effect based current probe (Tektronix A622) monitored the discharge evolution and the energy release across the electrodes. The fast dynamics of the discharge were tracked through measurements at 1 GHz during 100 μs with a LeCroy LT262 data acquisition system.

Figure 5 shows the voltage and electrical current during the arc discharge in the high voltage section of the circuit. The transition towards the breakdown took 50 μs and reached a value (5.5 kV)

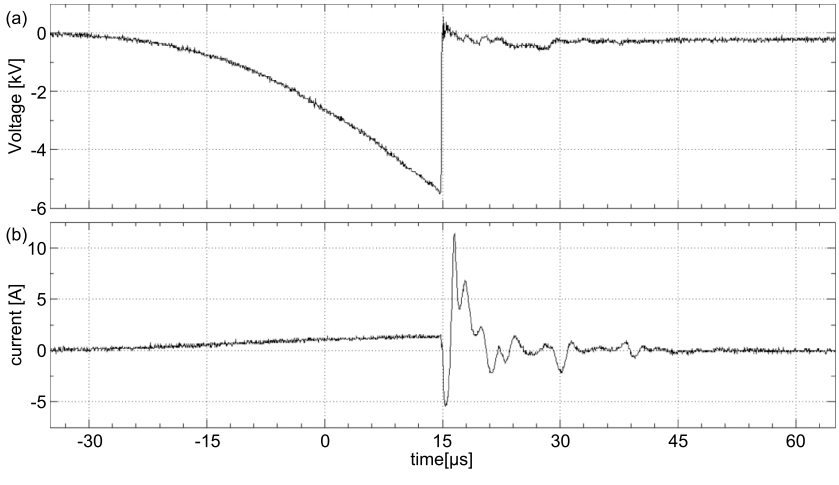

FIG. 5. Voltage (a) and current (b) measurements at the secondary windings of the coil during an arc discharge—the breakdown (5.5 kV) is achieved at 15 μs.

lower than the theoretical one (13.4 kV given by Paschen's law at atmospheric pressure[20]) owing to the electrode sharpening. The gradual decrease of voltage up to the breakdown threshold of 5.5 kV is followed by a steep increase that reinstated the voltage towards the base level. The smooth increase of the electrical current up to 1.6 A confirmed the transition towards the arc state. At the breakdown, a negative peak of current of 5.3 A corresponding to a positive peak of voltage revealed the negative ohmic nature of the air.[21] The current peak was slightly delayed with respect to the voltage apex because of the inductive nature of the circuit. The conductive state of the air after the breakdown resulted in a high current up to 11.4 A that was quickly damped in the following 30 μs. The electrical power is the result of the multiplication of the voltage and current trace displayed in Fig. 5. The energy release by the three electrode pairs at each pulse, computed from the integration of the power trace (Power = V × I), was 100 mJ. The measurement uncertainty from the manufacturers' datasheets is 4.1% for the current and 3.3% for the voltage while the accumulated uncertainty for the power is 5.3%.

III. LASER BASED DOUBLE SHOT SCHLIEREN SYSTEM

A. Illumination source and image capture

Reduction of the exposure time is essential to capture the flow phenomena in the visualization of high speed flows. This is conventionally accomplished through cameras with high sampling rates. However, an equivalent result can be achieved by narrowing the time of the illumination during the acquisition.[22] A novel concept used in this work was a PIV system for short exposure Schlieren imaging. PIV lasers usually produce pulses in the range of 5-9 ns with a time separation between two shots in the order of 0.6-2 μs. Therefore, two images can be recorded during a time interval that outperforms conventional high speed cameras.

The illumination for the current optical system was a New Wave Solo PIV I Nd:YAG pulsed laser producing laser light at wavelength of 532 nm with a pulse duration of 5 ns at 15 mJ energy. The PCO-sensicam branded double-shot version camera permitted a minimum time separation between two image recordings of 2 μs that resulted in 20 pixels displacement of the freestream flow structures. The current field of view was 73.2 × 59 mm that was resolved by 1280 × 1024 pixels.

The appearance of interference fringes on the Schlieren image due to the coherence of the laser light and the presence of the knife edge[23–26] was overcome using the phenomenon of Laser Induced Fluorescence (LIF). The fluorescent plate provided by a LaVision diffuser allowed to reach a fluorescent light duration of 20 ns, enough to produce a displacement of the flow structures less than one pixel during the exposure of the camera.[18]

The pair of correlated short exposure images permitted insight into the instantaneous dynamics of the flow. The turbulent structures of the boundary layer allowed the computation of a velocity profile in the boundary layer by using structure-based cross correlation algorithms.[26,27] The present measurement technique offers ancillary information to the conventional Schlieren visualizations, providing velocities of turbulent structures without the need to seed the flow but is inadequate to determine the flow velocity in the main stream.

B. Optical arrangement

Figure 6 depicts the arrangement of the Z-type Schlieren setup installed on the wind tunnel. Two parabolic mirrors provide the light beam across the test section equipped with two lateral quartz windows. The de-coherentized laser light beam was driven to the focal point of the first parabolic mirror through a planar mirror and a convergent lens. Moreover, a set of polarizing filters prior to the parabolic mirror prevented the saturation of the CCD sensor of the PCO camera.

The second parabolic mirror collected the light on the other side of the test section and delivered it to the focal point, where the knife edge was placed to enhance the density gradients within the test section. An achromatic doublet with a focal length of 160 mm converged the image directly on the CCD of the camera and prevented, at the same time, spherical aberration. The synchronization among the Schlieren system, the pressure measurement chain, and the electrical discharges was

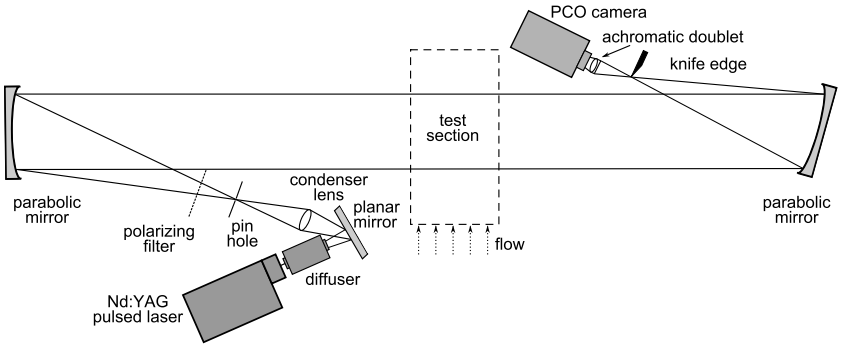

FIG. 6. Laser Schlieren setup.

achieved through a MotionPro Timing Hub synchronizer that received the trigger at the breakdown thanks to a Hall effect current sensor on the primary windings of the coils.

IV. RESULTS AND DISCUSSION

A. Quiescent conditions

1. Sound wave

The macroscopic effects of an electrical arc discharge are a sequence of three phenomena: light emission, sound wave propagation, and heat release. All of them occur at the breakdown but propagate at different speeds. The series of frames in Figure 7 allows to observe how the effects evolve in time and space. The pictures are characterized by an exposure time of 5 ns and report a magnified view of the electrode locations. A shock wave related to the sudden temperature rise was generated and propagated with a cylindrical shape, at the speed of sound corresponding to the air temperature (295.7 K).[4,28] The temperature around the electrodes was neither homogeneous

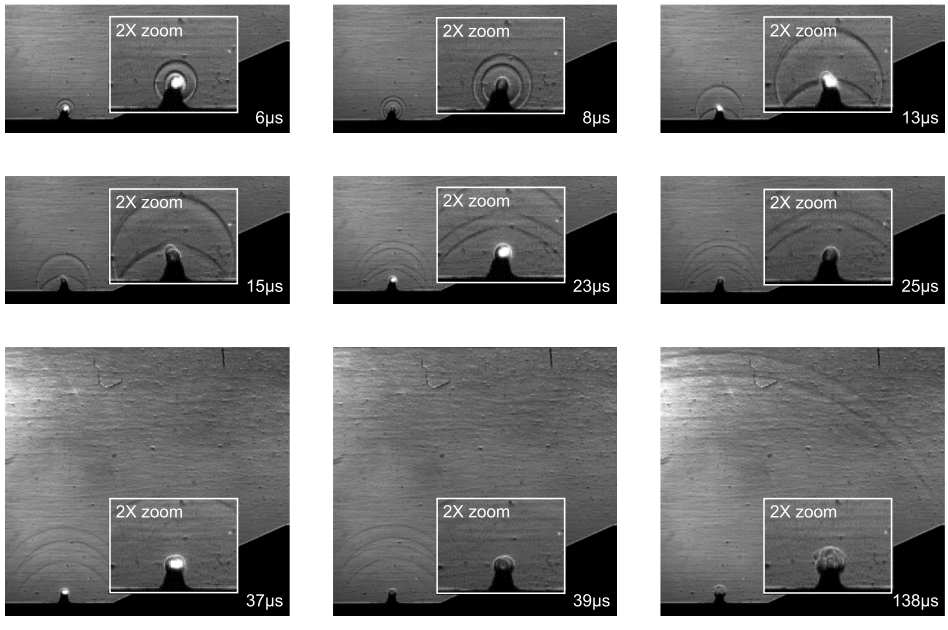

FIG. 7. Macroscopic effects of arc discharges in quiescent conditions.

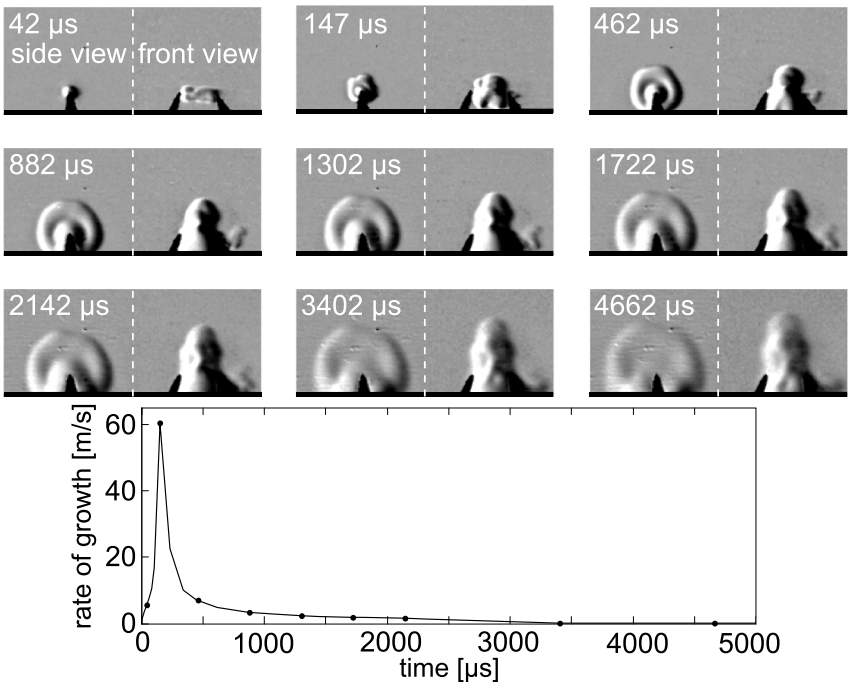

FIG. 8. Thermal effects of a discharge in quiescent conditions −256×128 pixels, exposure time 18.24 μs.

nor uniform in time. Hence, tiny variations of the speed of sound resulted in pressure waves being slightly decelerated as the radius increased and deformation of circular shape.

The first frames of Figures 7 show the sound waves propagating from the electrodes. The propagation speed of the sound wave computed using the magnification factor of the picture (0.0543 mm/pixel) was estimated to be 353 m/s, close to the thermodynamic speed of sound (345 m/s for dry air). To minimize the overlapping of the sound waves coming from each actuator, the central one was disabled and two wave patterns could be noticed. As the two sound waves reached the bottom surface of the test section, they were reflected upwards and propagated at the same speed but with a delay of 3.6 μs. The weakening of the pressure wave was confirmed by the gradual reduction in the pressure gradients through the propagation. Afterwards, the pressure effect of the discharges was replaced by the thermal interactions in the flow.

2. Thermal perturbation

The evaluation of the temperature perturbation induced by the DC discharges at quiescent flow conditions was accomplished through high speed Schlieren visualizations with multichromatic illumination. The time scale of the related thermal phenomenon is longer than the time scale of the pressure wave propagation and the glow. Hence, a relatively lower acquisition frequency (47 kHz) was chosen. The two frame series in Figure 8 report lateral and frontal views of the same phenomenon obtained in two separate experiments. The tests were performed rotating the actuator in quiescent conditions. After the discharge, the air surrounding the arc was exposed to a sudden increase of temperature. Therefore, the thermal distortion generated in between the electrode tips resembled the arc shape (42 μs) and further expanded because of the heat exchange with the colder air nearby. Initially, the shape of the hot region is cylindrical, being the axis of the cylinder at the electrodes tips. After the first 500 μs, we observe that this hot volume reaches the endwall support of the electrodes, and therefore, part of the heat will be dissipated into the actuator endwall. The disk of hot air caused by the discharge grows in size and rises due to buoyancy. As the hot region expands, the inner temperature lowers, which is highlighted by a weaker front in the Schlieren pictures observed after 3.4 ms. The rate of growth of the hot disk of air is represented in the lower

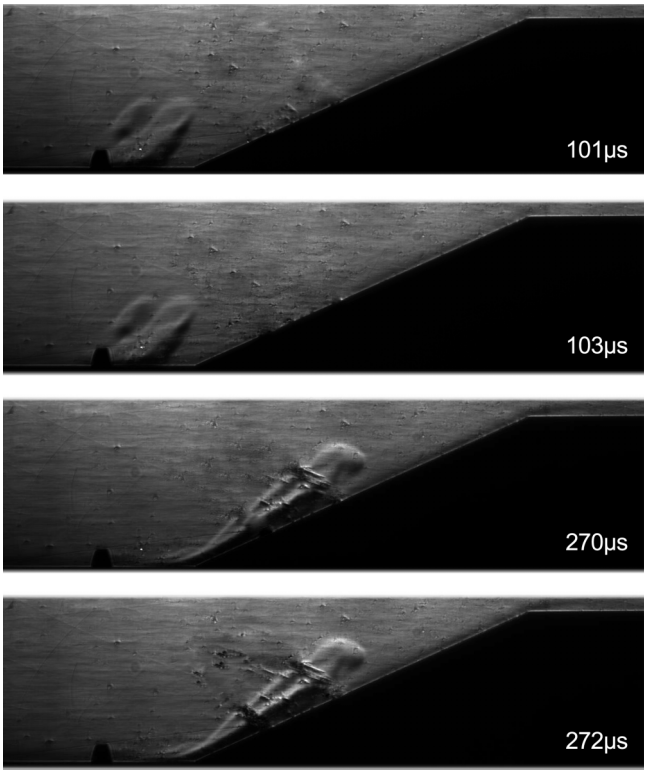

FIG. 9. Streamwise propagation of the thermal effects at low speed (Mach 0.33).

part of Figure 8 and shows a rapid propagation of the thermal perturbation up to 60 m/s in the early stages of the development due to the magnitude of the temperature differences between the hot air and environment. The radius of the hot disk of air reached 3.8 mm after 5 ms.

B. Low speed flow (M = 0.33)

Figure 9 shows the distortion of the high-temperature bubble during the blow down of the wind tunnel. The upward propagation of the temperature field shown in quiescent conditions combined with its motion in the streamwise direction imposed by the flow. Therefore, the region of hot air disseminated along the wedge with an extent proportional to the flow speed. The length of the thermal plume along the streamwise direction (i.e., the furthest length from electrode tip to extreme part of the hot plume) reached 11.6 mm at a flow speed of 115 m/s. The length of the thermal plume translated up to 31.1 mm from the electrodes around 170 μs later.

C. High speed flow (M = 3.3)

The experimental campaign in the supersonic regime was performed in three different conditions: without the electrodes, with their presence, and with the discharge actuation. Figure 10(d) shows the static pressure trend along the compression ramp for an upstream total pressure of 7 bar in the settling chamber of the wind tunnel, while Figures 10(a)-10(c) report the flow field in the three test cases, respectively. The vertical segment that appears at the top right of the frames is not a flow feature but due to a flaw in the optical windows. Assuming an isentropic expansion in the nozzle, from the static and total low frequency pressure measurements, a freestream Mach number of 3.3 was reached in the test section. Downstream of the oblique shock, inclined at 40.3°, the Mach number decreased to 1.97 along the streamwise direction. In the present configuration within the boundary layer, in the vicinity of the ramp shock, the prong induced hemispherical shock waves

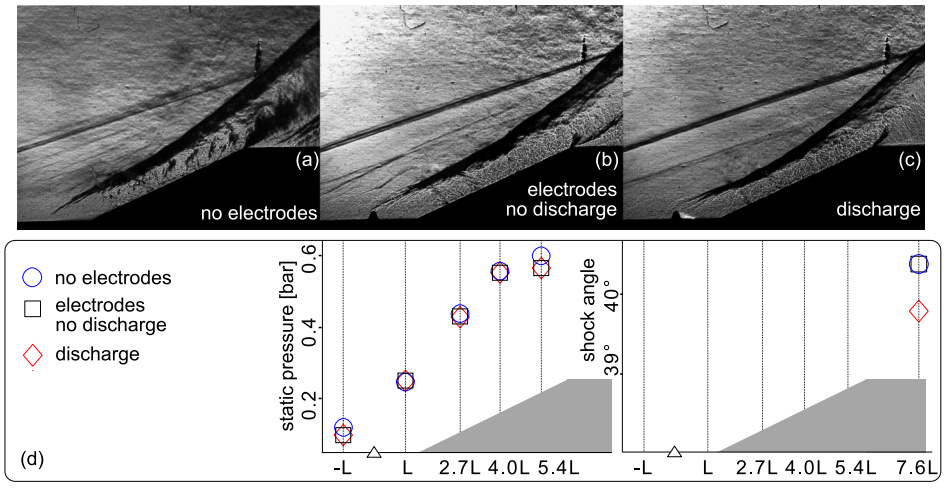

FIG. 10. Flow past a compression ramp at Mach 3.3 (a) clean configuration, (b) presence of the electrodes, (c) presence of arc discharges, (d) wall static pressure evolution and oblique shock angle (reference length L = 7 mm, measures at 7.6 L) with p_{01} 7 bars—(the vertical segment on the top right is a scratch on the window).

may help to anchor the unsteady ramp shock. Furthermore, since they were located concurrently with the shock foot, the actuations could be supplied in a high sensitivity region of the flow field.

The effects of arc discharges in supersonic conditions were quantitatively analyzed through cross correlation algorithms on the consecutive picture couples. The nano-second exposure time and the high resolution of the pictures enhanced the sharpness of the turbulent structures which were used as the trackers. As highlighted in Figure 11(a), the region investigated was the flow along the ramp downstream of the oblique shock wave. The frames were rotated to make the leading edge of the ramp horizontal and further cropped in a region of 720×100 pixels as depicted in Figure 11(b), with two consecutive frames ready to process. Moreover, during the image pre-processing, a mask was applied on the upper part of the picture that still showed the shock wave. The interrogation windows had to be stretched along the direction of the dominant flow. The aspect ratio of the interrogation windows was 4 (256/64 pixels). The software used for the cross-correlation computation is an in-house code, window deformation iterative multigrid that determines the velocity vectors in the interrogation windows by taking into account shear and rotation effects. In order to refine the vector field, we refined the interrogation windows in multiple steps and the vector field of the coarser grid of interrogation windows is used as a predictor for the next, finer grid of the interrogation windows. The two levels of refinement mean that the first interrogation window size was 256×64 pixels, the first refinement level was 128×32 pixels, the second and last refinement level was 64×16 pixels. For the last and finest refinement level, overlapping was applied during the processing with an amount of 48 pixels over 64 pixels that means 75% of overlapping in the main flow (horizontal) direction, while 12 pixels overlapping on 16 pixels windows, i.e., also 75% overlapping was applied for the wall normal direction. The final vector spacing was thus 4 pixels in wall normal and 16 pixels in the main flow direction (horizontal). This gives 45 vectors in horizontal and 25 vectors in wall normal direction, in total 1125 vectors. The totality of these vectors is used for the construction of the histograms reported in the paper.

Figure 11(c) reports the velocity field computed processing ten picture couples for the three configurations (no electrodes, electrodes without discharges, and discharges). From all results, a clear tendency was observed on the evolution of the velocity magnitude from one configuration to another. As depicted in Figure 11(c), the velocity magnitude increased with the presence of the electrodes. A histogram of velocity magnitude was built considering values above 360 m/s to analyze the effect of the discharges on the velocity field. The velocity range in the figure was selected to highlight the difference among the three configurations of about 20 m/s around the mean level. The number of velocity vectors included in each class was normalized by the total number of vectors.

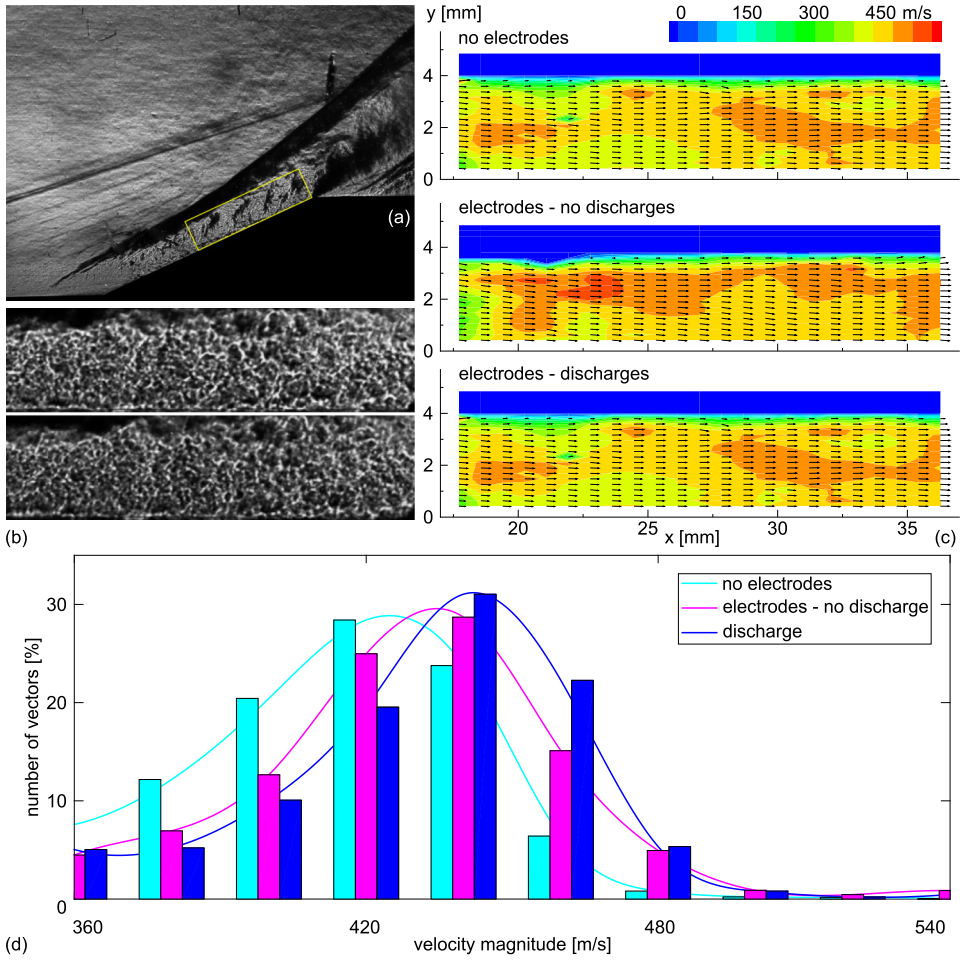

FIG. 11. Image processing by cross correlation on the boundary layer velocity field (M = 3.3): Region Investigated (a), Turbulent structures along the ramp (720×100 pixels) with the discharge (b), Velocity field inside the turbulent boundary layer (c), Velocity magnitude histogram (d).

The displayed results were averaged over the ten sets of frames processed for each configuration (Figure 11(d)). The comparison between the three configurations shows that the velocity distribution tends to follow a skewed Gaussian trend that is translated to higher velocities in the presence of the electrodes and even more in the presence of discharges through the averaged velocity magnitudes over the ten sets of frames of 454, 476 and 492 m/s respectively. The implementation of the prongs caused a local blockage within the boundary layer, which results in flow acceleration of 22 m/s. The occurrence of the arc, and in particular the thermal effect, causes the appearance of a hot disk that further accelerated the flow 16 m/s. The uncertainty in the estimation of the velocity is less than 2 m/s.

The results confirm the effect of the low energy electrical discharges (100 mJ per pulse for all the actuators) on the high energy flow field (30 J), and in particular on the propagation of the turbulent structures along the wedge. The shadowgraph and Schlieren image velocimetry results presented by Jonassen *et al.*[26] in conditions similar to our present research exhibited a very good agreement with Pitot probe surveys.

The determination of the uncertainty in the velocity was evaluated numerically by applying synthetic perturbations to the real images.[26,29,30] As a result of the experiments, one obtains image pairs that contain a certain displacement of the structures. To determine how precisely the correlation algorithm can determine the displacement, i.e., what is the sensitivity of the method, one can impose exact, artificial displacement of the structures on the existing images and verify what

TABLE I. Summary of velocity measurement uncertainties.

Error source	Mean (m/s)	Dispersion (m/s)
Self shift image A (280×54 pixels)	±0.37	±0.21
Self shift image B (280×54 pixels)	±0.33	±0.24

the correlation algorithm yields. One image pair consists of two images: image A and image B. First, an artificial shift of approximately the same magnitude as was measured (15-20 pixels) in the mean flow direction was performed for all the A images of the series. This investigation is referred to as self shift tests, because in this case, one cross-correlates the given image with itself shifted by a known number of pixels. The same self shift tests were also carried out on all the B images of the series. The self shift tests were carried out in both the mean flow (x) direction and wall normal (y) direction. It has been found that the error of the correlation is somewhat higher in the normal direction to the wall than along the streamwise direction which is related to the ratio of the size of the density structures and the size of the interrogation windows in the wall normal (y) direction.

In order to take into account also the evolution of the density structures as well as the variation of laser intensities of the two laser cavities, the images B of the series were perturbed by 1–4 pixels shifts in the x and y directions and the images obtained in this way were correlated with the corresponding A images. In this test case, the velocity field is not homogeneous, but it is homogeneously perturbed. It is then possible to determine the error of the correlation in the lower and higher speed zones. The maximum error obtained from the self shift tests was 0.659 m/s, while from the perturbation of the B image series, it was 1.845 m/s. The mean error and the standard deviation are below these values and are listed in Table I for self shift images A and B.

V. CONCLUSIONS

The influence of DC arc discharges on the flow fields at various speed regimes was investigated through experimental measurements assessing their capability as an active flow control technique. Indeed, electrical arc discharges could be easily tuned with the flow field acting on the frequency and on the power of the actuations. In the current work, the configuration tested was a ramp with an electrode array at the point of contraction, where the oblique shock wave originated. Nevertheless, additional investigations were done in quiescent and subsonic conditions.

High-speed visualizations during the discharge revealed the cathode erosion and the further aging of the support that lost its dielectric properties. An improved design with tungsten electrodes slanted inside a machinable glass ceramic support prevented these issues and provided aligned discharges perpendicular to the flow direction. Furthermore, an electronic circuit based on automotive ignition coils guaranteed the synchronization of discharges. Electrical measurements at the low and high voltage sections of the circuit allowed to characterize the discharge evolution and to estimate the amount of the energy release into the flow during each actuation.

The detailed flow visualization of the discharges was achieved, thanks to the development of a high speed short exposure Schlieren imaging technique. It relies on a pulsed laser and a PIV camera that were able to provide exposure times as low as 5 ns. A fluorescence based light conversion with Rhodamine B removed the fringe patterns caused by the coherence of the laser and led to a uniform good quality Schlieren image. This technique allowed to capture the three macroscopic effects associated with an arc discharge: light emission, shock wave propagation at the local speed of sound and heating.

The residence time of the thermal perturbations observed was two orders of magnitude slower than the pressure effects. The Joule effect, when the arc state was reached, heated the air nearby and expanded with a cylindrical shape. The momentum entrained by the flow further spread this region in the streamwise direction.

In supersonic conditions, the residence time of the effects induced by the electrical discharges needed an unconventional analysis to achieve the flow field characterization with and without the actuations. The algorithms usually implemented for cross correlation analyses were adopted without seeding the flow but using the turbulent structures that develop behind the oblique shock wave as trackers. In spite of the low energy applied (only 100 mJ per pulse for all the 3 actuators), we could observe the ability of the technique to modify the turbulent structures underneath the shock waves. These conclusions are important to consider future actuation technology, and how we could effectively modify the flow patterns.

ACKNOWLEDGMENTS

The authors are grateful to Mr. Adrien Pertat for his contribution during the tests as well as during the data processing.

[1] A. Bogaerts, E. Neyts, R. Gijbels, and J. van der Mullen, "Gas discharge plasmas and their applications," Spectrochim. Acta, Part B **57**(4), 609–658 (2002).
[2] L. B. Loeb and J. M. Meek, "The mechanism of spark discharge in air at atmospheric pressure. I," J. Appl. Phys. **11**(6), 438–447 (1940).
[3] J. Zeleny, "The mechanism of the electric spark," J. Appl. Phys. **13**(7), 444–450 (1942).
[4] R. A. Freeman and J. D. Craggs, "Shock waves from spark discharges," J. Phys. D: Appl. Phys. **2**(3), 421 (1969).
[5] R. F. Haley and P. R. Smy, "Electrically induced turbulence-the short duration spark," J. Phys. D: Appl. Phys. **22**(2), 258 (1989).
[6] L. N. Cattafesta and M. Sheplak, "Actuators for active flow control," Annu. Rev. Fluid Mech. **43**(1), 247–272 (2011).
[7] M. L. Post, T. C. Corke, S. Wilkinson, D. Ashpis, D. Miller, and L. Ukeiley, "Separation control on high angle of attack airfoil using plasma actuators," AIAA J. **42**(11), 2177–2184 (2004).
[8] M. Nishihara, N. Jiang, J. W. Rich, W. R. Lempert, I. V. Adamovich, and S. Gogineni, "Low-temperature supersonic boundary layer control using repetitively pulsed magnetohydrodynamic forcing," Phys. Fluids **17**(10), 106102 (2005).
[9] M. Samimy, J. Kim, J. Kastner, I. Adamovich, and Y. Utkin, "Active control of high-speed and high-Reynolds-number jets using plasma actuators," J. Fluid Mech. **578**, 305–330 (2007).
[10] S. Leonov, D. Yarantsev, and V. Sabelnikov, "Electrically driven combustion near the plane wall in a supersonic duct," Prog. Propul. Phys. **2**, 519–530 (2011).
[11] S. Leonov, V. Bityurin, K. Savelkin, and D. Yarantsev, "Progress in investigation for plasma control of duct-driven flows," in *41st Aerospace Sciences Meeting and Exhibit* (American Institute of Aeronautics and Astronautics, Reno, 2003), Vol. 699.
[12] M. Samimy, I. Adamovich, B. Webb, J. Kastner, J. Hileman, S. Keshav, and P. Palm, "Development and characterization of plasma actuators for high-speed jet control," Exp. Fluids **37**(4), 577–588 (2004).
[13] C. Hahn, M. Kearney-Fischer, and M. Samimy, "On factors influencing arc filament plasma actuator performance in control of high speed jets," Exp. Fluids **51**(6), 1591–1603 (2011).
[14] B. DeBlauw, C. Dutton, and G. Elliott, "A Mach 4 wind tunnel for plasma/boundary layer interaction studies," in *48th AIAA Aerospace Sciences Meeting Including the New Horizons Forum and Aerospace Exposition* (American Institute of Aeronautics and Astronautics, Orlando, 2010), Vol. 1485.
[15] B. DeBlauw, E. Lazar, N. Kale, N. Glumac, C. Dutton, and G. Elliott, "Flow and thermal properties induced by electric arc plasma actuators," in *49th AIAA Aerospace Sciences Meeting Including the New Horizons Forum and Aerospace Exposition* (American Institute of Aeronautics and Astronautics, Orlando, 2011), AIAA Paper AIAA 2011-734, Vol. 734.
[16] T. M. Reedy, N. V. Kale, J. C. Dutton, and G. S. Elliott, "Experimental characterization of a pulsed plasma jet," AIAA J. **51**(8), 2027–2031 (2013).
[17] E. Caraballo, N. Webb, J. Little, J. Kim, and M. Samimy, "Supersonic inlet flow control using plasma actuators," in *47th AIAA Aerospace Sciences Meeting Including The New Horizons Forum and Aerospace Exposition* (American Institute of Aeronautics and Astronautics, Orlando, 2009), AIAA Paper AIAA 2009-924, Vol. 924.
[18] T. Regert, G. Grossir, S. Paris, and L. Blay Esteban, "Schlieren visualization for high-speed flows based on laser-induced fluorescence," Exp. Fluids **55**(2), 1–6 (2014).
[19] F. L. Jones, "Electrode erosion by spark discharges," Br. J. Appl. Phys. **1**(3), 60 (1950).
[20] F. Paschen, "Ueber die zum funkenbergang in luft, wasserstoff und kohlensure bei verschiedenen drucken erforderliche potentialdifferenz," Ann. Phys. **273**(5), 69–96 (1889).
[21] J. D. Cobine, *Gaseous Conductors: Theory and Engineering Applications* (Dover Publications, New York, NY, 1958).
[22] K. M. Casper, S. J. Beresh, J. F. Henfling, R. W. Spillers, and B. O. M. Pruett, "High-speed Schlieren imaging of disturbances in a transitional hypersonic boundary layer," in *51st AIAA Aerospace Sciences Meeting,* (American Institute of Aeronautics and Astronautics, Grapevine, 2013), AIAA Paper AIAA 2013-376, Vol. 376.
[23] P. K. Panigrahi and K. Muralidhar, *Schlieren and Shadowgraph Methods in Heat and Mass Transfer* (Springer, 2012), Vol. 2.
[24] D. S. Hacker and F. D. Hussein, "The application of a laser-Schlieren technique to the study of single bubble dynamics," Ind. Eng. Chem. Fundam. **17**(4), 277–283 (1978).
[25] F. Shugaev, S. Bystrov, and E. Fomenko, "The use of a laser Schlieren technique for the investigation of the shock structure in high-frequency discharge plasma," J. Flow Visualization Image Process. **1**(1), 59–61 (1993).

[26] D. R. Jonassen, G. S. Settles, and M. D. Tronosky, "Schlieren PIV for turbulent flows," Opt. Lasers Eng. **44**(34), 190–207 (2006).
[27] I. A. Horvath, "Extreme PIV applications: Simultaneous and instantaneous velocity and concentration measurements on model and real scale car park fire scenarios," Ph.D. thesis (Université Libre de Bruxelles, 2012).
[28] F. Tholin, "Numerical simulation of nanosecond repetitively pulsed discharges in air at atmospheric pressure: Application to plasma-assisted combustion," Ph.D. thesis (École Centrale Paris, 2012).
[29] M. Raffel, C. Willert, and J. Kompenhans, "Post-processing of PIV data," in *Particle Image Velocimetry*, Exp. Fluid Mech. (Springer, Berlin, Heidelberg, 1998), pp. 147–171.
[30] B. F. Bathel, P. M. Danehy, J. A. Inman, S. B. Jones, C. B. Ivey, and C. P. Goyne, "Multiple velocity profile measurements in hypersonic flows using sequentially-imaged fluorescence tagging," in *48th AIAA Aerospace Sciences Meeting Including the New Horizons Forum and Aerospace Exposition* (American Institute of Aeronautics and Astronautics, Orlando, 2010), AIAA Paper AIAA 2010-1404, Vol. 1404.